ELSEVIER

Contents lists available at ScienceDirect

Computer Methods and Programs in Biomedicine

journal homepage: https://www.sciencedirect.com/journal/computer-methods-and-programs-in-biomedicine



Multiscale simulation and parallel space–time adaptivity of calcium sparks in cardiac myocytes



Wilhelm Neubert ^a, Martin Falcke ^{a,b}, Nagaiah Chamakuri ^c

- ^a Max Delbrück Center for Molecular Medicine in the Helmholtz Association, Berlin, Germany
- ^b Humboldt University Berlin, Institute of Physics, Berlin, Germany
- c School of Mathematics & Center for HPC, Indian Institute of Science Education and Research Thiruvananthapuram, Thiruvananthapuram, India

ARTICLE INFO

Keywords: Calcium release units Finite Element Method Calcium cycling Cardiac myocyte Space-time adaptivity Adaptive Runge-Kutta methods

ABSTRACT

Background and Objective: Calcium serves as the bidirectional link between the heart's electrical excitation and contraction. Electrical excitation induces an influx of Calcium across the sarcolemma and T-tubular membrane, triggering calcium release from the sarcoplasmic reticulum. Calcium sparks, the fundamental events of calcium release from the SR, are initiated in specialized microdomains where Ryanodine Receptors and L-type calcium channels co-locate. The spatial heterogeneity of Calcium release and the random occurrence of strong release fluxes render simulations challenging. Developing mathematical models and efficient simulations of detailed calcium spark models is crucial to understanding heart function. In this paper, we introduce space-time adaptivity within a parallel computing framework into the multiscale simulation of calcium sparks in cardiac myocytes to improve the stability and performance of these simulations.

Methods: We model intracellular calcium concentrations in both the cytoplasm and the SR domains using a set of coupled reaction–diffusion equations. Spatial grid adaptivity is implemented through multilevel finite element methods to account for the spatial heterogeneity of intracellular Ca^{2+} release. Rosenbrock-type techniques handle small time steps for simulating stochastic channel opening and closing in the Ca^{2+} release units (CRUs).

Results: Our test cases demonstrate the superior efficiency of the space–time adaptive approach in optimizing computational resources. The parallel space–time adaptive method accelerates simulations of calcium sparks by a factor of 16.07.

Conclusions: The efficiency and speed gains in Calcium spark simulations are significant and enable modeling based research into previously difficult to tackle questions with regard to sub-micrometer scale models, e.g with respect to local interactions between the Sodium Calcium Exchanger and RyR clusters.

1. Introduction

Biomedical research often relies on understanding the functional implications of molecular changes on the entire biological system. This necessitates a mechanistic comprehension of the interactions between different scales from molecular to cellular behavior, often achieved by multi-scale simulations. Calcium (Ca^{2+}) is central to heart contraction, acting as the bidirectional link between the heart's electrical excitation and contraction. Electrical excitation triggers Ca^{2+} influx across the sarcolemma and T-tubular membrane, leading to calcium release from the sarcoplasmic reticulum (SR), a membrane-bound Ca^{2+} storage compartment. Ca^{2+} sparks, the fundamental events of this calcium release, are crucial for understanding heart function. Sparks are brief,

lasting 10 to 100 ms. They are generated by clusters of Ryanodine receptor channels (RyRs) which release Ca²⁺ from the SR inside dyadic clefts, which are formed by SR- and T-tubule membrane being as close as 15 nm inside CRUs (see Fig. 1). Consequently, computational modeling efforts to explore such multi-scale systems must incorporate various spatial and temporal scales to be effective. This study focuses on space–time adaptivity exemplified by a multi-scale model of the excitation–contraction coupling process of cardiomyocytes.

Cardiomyocytes contract when Ca²⁺ binds to the sarcomeres. These are longitudinally arranged protein structures that are bounded by z-discs on either end. T-tubules are invaginations of the extracellular space into the myocytes. Specialized junctional subvolumes of the SR

^{*} Corresponding author at: Max Delbrück Center for Molecular Medicine in the Helmholtz Association, Berlin, Germany.

E-mail addresses: wilhelm.neubert@mdc-berlin.de (W. Neubert), martin.falcke@mdc-berlin.de (M. Falcke), nagaiah.chamakuri@iisertvm.ac.in (N. Chamakuri).

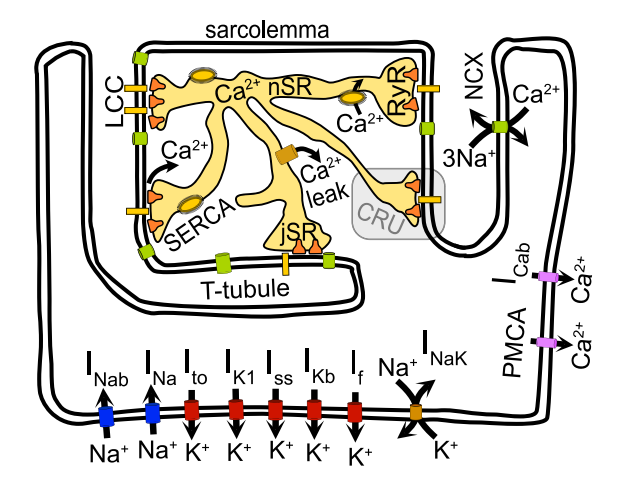


Fig. 1. Structures within z-discs involved in $\operatorname{Ca^{2+}}$ dynamics and the currents defining the rat electrophysiology model. T-tubules are invaginations of the plasma membrane reaching deep into the bulk of the cell. The sarcoplasmic reticulum (SR) stores $\operatorname{Ca^{2+}}$ and consists of network SR (nSR) and junctional SR (jSR) compartments. $\operatorname{Ca^{2+}}$ release units (CRUs) with their L-type $\operatorname{Ca^{2+}}$ channels (LCCs) and Ryanodine receptor channels (RyRs) are formed by T-tubule and jSR membrane. RyRs release $\operatorname{Ca^{2+}}$ from the jSR. The $\operatorname{Na^{+}}/\operatorname{Ca^{2+}}$ -exchanger (NCX) and the plasma membrane $\operatorname{Ca^{2+}}$ -ATPase (PMCA) transport $\operatorname{Ca^{2+}}$ across the sarcolemma and T-tubule membrane. The electrophysiology model includes additionally the $\operatorname{Na^{+}}$ current $\operatorname{I}_{Na^{+}}$, the background $\operatorname{Na^{+}}$ current $\operatorname{I}_{Ka^{+}}$, the inward rectifier $\operatorname{K^{+}}$ current $\operatorname{I}_{K1^{+}}$, the background $\operatorname{K^{+}}$ current $\operatorname{I}_{K2^{+}}$, the inward rectifier $\operatorname{K^{+}}$ current $\operatorname{I}_{K1^{+}}$, the background $\operatorname{K^{+}}$ current $\operatorname{I}_{K2^{+}}$, the steady state outward $\operatorname{K^{+}}$ current $\operatorname{I}_{K2^{+}}$, the hyperpolarisation activated $\operatorname{K^{+}}$ current $\operatorname{I}_{F1^{+}}$, the $\operatorname{Na^{+}}/\operatorname{K^{+}}$ -ATPase $\operatorname{I}_{N2^{+}}$, and the background $\operatorname{Ca^{2+}}$ current $\operatorname{I}_{C2^{+}}$.

(jSR) come in close proximity to T-tubule membrane and form CRUs. CRUs are concentrated in the z-discs (see Fig. 1). The jSR wraps around the T-Tubules, leaving clefts of around 15 nm between the two membranes. In these narrow dyadic clefts, two groups of channels form clusters opposite each other: On the sarcolemmal side are the Ltype Ca²⁺ channels (LCCs). They are voltage gated and Ca²⁺ inhibited channels that allow Ca²⁺ to enter the dyadic space upon depolarization of the plasma membrane. Opposite the LCCs in the jSR membrane is a cluster of RyRs. They are activated by dyadic Ca²⁺ and release Ca²⁺ from the jSR store. The triplet of dyadic space, the Ca²⁺ channels, and the jSR compartment is called a Calcium Release Unit (CRU). During electrical stimulation, a small Ca²⁺ influx into the dyadic space by LCCs triggers a much larger release of Ca²⁺ by the RyRs. The released Ca²⁺ diffuses out of the dyadic space and through the cytosol towards the sarcomeres to trigger contraction. The process in the CRUs is called Calcium induced Calcium Release (CICR). It is the essential translation and amplification step from electric to Ca²⁺ signal that enables excitation-contraction coupling (ECC) in cardiac myocytes. Each z-disc contains around 400 CRUs, and each cardiomyocyte consists of around 50 z-discs with gaps of $\sim 2\mu m$ between them.

Ca²⁺ gradients inside and around CRUs during sparks are steep and local Ca²⁺ concentrations reach many times the base level. Sparks are highly random events. Locally, they can be considered as shotnoise-like events due to the large concentration amplitudes and the temporal randomness. Hence, we cannot approximate sparks by spatial averaging and deterministic dynamics. Simulating the initiation, termination, and regulation of calcium sparks typically requires significant computational resources. This study aims to reduce computational time and memory usage by leveraging space–time adaptivity, which is particularly efficient given the infrequent channel events in spark simulations.

Sparks are of special interest for research on ECC since they allow for studying RyR, jSR, and LCC dynamics [1–3]. Additionally, sparks may occur as perturbations of SR Ca²⁺ cycling during the contraction

cycle, causing pathological arrhythmogenic membrane depolarizations. In particular, the latter role requires multi-scale simulation skills.

Constructing a multiscale model to represent these processes across different temporal and spatial scales is challenging [4]. Our multiscale model encompasses the various biophysical processes involved in excitation–contraction coupling in cardiomyocytes. It includes ion channel transitions that occur in tenths of milliseconds and spatial scales of tens of nanometers, as well as whole-cell electrophysiology spanning several seconds and spatial scales up to 100 micrometers (see Fig. 2).

Various adaptivity approaches have been demonstrated to significantly reduce the computational cost of simulating reaction–diffusion models compared to the use of structured grids [5–12]. Furthermore, the dynamic load balancing of such space–time adaptivity has been discussed in previous studies [12,13]. Nagaiah et al. used adaptivity in both space and time for the numerical simulation of stochastic and deterministic equations for intracellular calcium dynamics in nonmuscle cells and in two dimensions [14]. However, limited work has focused on the simulation of calcium dynamics in cardiac myocytes. This paper aims to enhance numerical simulations of calcium dynamics by focusing on this critical ability. In our recent work [15], we presented a mathematical modeling and computational approach for simulating intracellular calcium dynamics in cardiac myocytes using static mesh and adaptive time-stepping strategies for multiple action potential simulations.

This study utilizes a conforming multilevel finite element method for spatial discretization and higher-order Rosenbrock methods for temporal discretization. Spatial grid adaptivity is achieved through Zienkiewicz and Zhu's error estimator [16], which computes the average of local solution gradients. An automatic step-size selection algorithm based on classical embedding ensures optimal accuracy. The simulation framework is developed based on the open source FEM framework DUNE [17].

The remainder of the paper is organized as follows: In Section 2.1.1, we begin by discussing the mathematical modeling of calcium dynamics, providing a comprehensive overview of the key components that drive the system. This includes a detailed formulation of the dynamics of the calcium release unit (CRU) and an in-depth description of the membrane potential model, which are critical to understanding the underlying processes governing calcium signaling. Section 2.2 presents the numerical methodologies employed for the space-time discretization. We provide a thorough explanation of the discretization techniques, with a particular focus on the space adaptivity, which allows for efficient resolution of localized phenomena, and the parallelization strategies implemented to improve computational performance. In Section 3, we present the results of the numerical simulations demonstrating the effectiveness of the space-time adaptivity in calcium spark simulations. A comparison of the simulation outcomes with and without space-time adaptivity is provided. Finally, in the last section, we summarize the study's key findings and discuss potential directions for future research.

2. Methods

2.1. Mathematical modeling

2.1.1. PDE model

We denote the cell volume by $\Omega \subset \mathbb{R}^3$ and the plasma membrane, i.e., its boundary, by Γ . The space–time cylinder of the computational domain is denoted by $Q = \Omega \times (0,T]$.

Cytosolic calcium model: The dynamics of the cytosolic Ca^{2+} concentration, c, comprise plasma membrane transport, release, and uptake by the SR and binding to buffers. Plasma membrane transport is carried by the voltage-controlled ion channels and the Na⁺/Ca²⁺-exchanger. The T-tubule network is an interface to extracellular fluid in the bulk of the cytosol, enabling membrane molecules like the

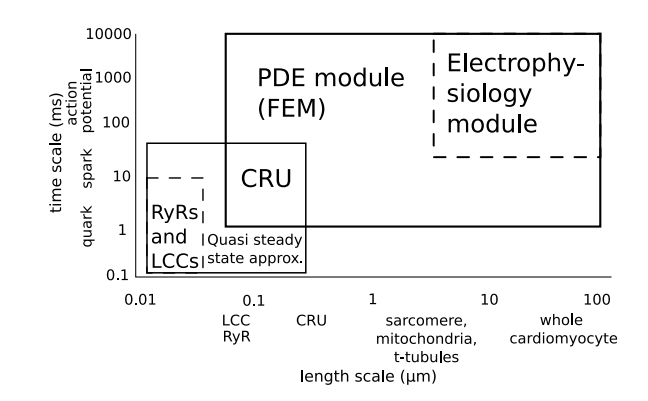


Fig. 2. The multiscale model covers several scales of biophysical processes during excitation–contraction coupling in cardiomyocytes. These include ion channel transitions in the order of 10th of milliseconds and on spatial scales of 10th of micrometers, as well as whole cell electrophysiology in the order of several seconds and spatial scales of up to $100~\mu m$. Using an experimentally measured approach, spontaneous calcium release events called spark-up to whole cell calcium waves can be simulated.

Table 1 Variables and fluxes of the PDE system. Plasma membrane Ca^{2+} ATPase flux and Ca^{2+} background flux are set to 0 in the version of the model simulated in this study.

Variable	Description
c b_s b_m	free cytosolic [Ca ²⁺] concentration of Ca ²⁺ bound stationary buffer in the cytosol concentration of Ca ²⁺ bound mobile buffer in the cytosol
$b_f S$	concentration of Ca ²⁺ bound fluorescent buffer in the cytosol free SR lumenal [Ca ²⁺]
Flux	Description
$egin{aligned} J_{cru} & J_{NaCa} \ J_{NaCa} \ J_{Pam} & J_{leak} \ J_{pump} \ J_{JSR} \ R_j \end{aligned}$	Ca ²⁺ bulk cytosol flux caused by CRUs bulk NCX Ca ²⁺ flux plasma membrane NCX Ca ²⁺ flux network SR Ca ²⁺ leak flux network SR Ca ²⁺ uptake by SERCAs Ca ²⁺ flux between network SR and JSR compartments reactions of free Ca ²⁺ with buffers $j = s, m, f$

Na⁺/Ca²⁺-exchanger to contribute to bulk concentration dynamics (J_{NaCa}) . The term J_{pump} describes the pumping of Ca²⁺ by SERCAs into the SR. The Ca²⁺ -binding molecules $(b_j, j = s, m, f)$ in the cytosol include stationary (s), mobile (m), and fluorescent (f) Ca²⁺ buffers. The total concentration b_j^{tot} is conserved for all buffers. The reaction terms $R_j(c,b_j)$ describe buffering of cytosolic Ca²⁺. For a short glossary of the used variables see Table 1. The partial differential equations for the cytosolic concentration fields read

$$\frac{\partial c}{\partial t} = \nabla \cdot \left(\mathbf{D_c} \nabla c\right) + J_{\mathrm{cru}} + J_{\mathrm{NaCa}} + J_{\mathrm{leak}} - J_{\mathrm{pump}} - \sum_{j=m,s,f} R_j \left(c,b_j\right) \ \ \mathrm{in} \ Q,$$

$$\frac{\partial b_{j}}{\partial t} = \nabla \cdot (\mathbf{D}_{\mathbf{b}_{j}} \nabla b_{j}) + R_{j} \left(c, b_{j} \right), \quad j = m, s, f \quad \text{in } Q.$$
 (2)

where $\mathbf{D_c} = \mathrm{diag}(D_c, D_c, D_c)$ and $\mathbf{D_{b_j}} = \mathrm{diag}(D_{b_j}, D_{b_j}, D_{b_j})$ are diagonal diffusion matrices. The expressions for the fluxes are

$$J_{\text{cru}} = \sum_{i=1}^{N_c} \Theta(|\vec{r} - \vec{r_i}| - r_{cru,i}) J_c^i(c, V, t),$$
(3)

$$J_{\text{leak}} = V_l(S - c),\tag{4}$$

$$J_{\text{pump}} = \frac{V_P^{\text{max}} c}{K_P + c} \frac{S_0}{S},\tag{5}$$

$$R_{j}\left(c,b_{j}\right)=k_{j}^{+}\left(b_{j}^{tot}-b_{j}\right)c-k_{j}^{-}b_{j}, \text{ where } j=s,m,f. \tag{6}$$

 ${
m Ca}^{2+}$ influx through LCC $(J^i_{
m LCC})$ and release through RyR $(J^i_{
m RyR})$ channels occurs mainly in dyadic clefts, see [15] for more details. They behave in a highly stochastic manner and will be described in detail in Section 2.1.2. The dependence on time of $J_{
m cru}$ is caused by this stochastic behavior.

We included a fluorescent buffer to emulate the approximation of $[Ca^{2+}]_i$ as it would be measured by a single wavelength Fluo-4 experimental recording using an *in vitro* calibration approach as described in [18]

$$[Ca^{2+}]_i^{exp} = K_d \frac{F - F_{\min}}{F_{\max} - F},$$
(7)

where K_d is the dissociation constant of Fluo-4, F is the experimentally measured fluorescence intensity, which is here set to the spatial average of b_f , $F_{\rm max}$ is the measured fluorescence intensity in Ca²⁺-saturated dye, which is here set to $b_f^{\rm tot}$, and $F_{\rm min}$ is the measured fluorescence intensity in the absence of Ca²⁺, which is here set to zero.

We describe the space inside CRUs as a flat cylinder in the detailed CRU model explained in Section 2.1.2. The interface between dyadic space and cytosol through which $\operatorname{Ca^{2+}}$ leaves the CRU is a band twisted in 3 dimensions since the junctional SR wraps around T-tubules. Since we cannot represent the shape of this interface for each CRU on the level of PDEs, we approximate its geometry as spherical source volumes centered at $\vec{r_i}$ with radius $r_{\operatorname{cru},i}$ and random fluxes $J_c^i\left(C(r_i),V,t\right)$. The flux $J_c^i\left(c,V,t\right)$ is the sum of all single channel LCC- and RyR-currents in the ith CRU divided by $4\pi r_{\operatorname{cru},i}^2/3$.

The boundary conditions for the above PDEs are given by the plasma membrane ${\rm Ca^{2+}}\text{-}{\rm currents}$ and are described by the following equations

$$\vec{n} \cdot \mathbf{D}_c \nabla c = J_{N, c, c, c}^{pm} \text{ on } \Gamma \times [0, T],$$
 (8)

$$\vec{n} \cdot \mathbf{D_{b_i}} \nabla b_j \qquad = 0 \text{ on } \Gamma \times [0, T] \qquad , \tag{9}$$

where J_{NaCa}^{pm} is the plasma membrane part of the Na⁺/Ca²⁺-exchanger flux [19].

Sarcoplasmic Reticulum (SR) calcium model: Ca²⁺ is released into dyadic clefts from individual jSR compartments. They are coupled by a diffusional flux

$$J_{JSR} = \sum_{i=1}^{N_c} \Theta(|\vec{r} - \vec{r_i}| - r_{s,i}) I_{\text{refill},i} / (4\pi r_{s,i}^3 / 3)$$
 (10)

to the network SR, which will be explained in more detail in Section 2.1.2. $I_{\text{refill},i}$ is defined in Eq. (13) and denotes the current from the network SR to the *i*th jSR. The radius of the sink volume in the lumen of the SR is $r_{s,i}$. This flux contributes to SR Ca²⁺ concentration (S) dynamics

$$\frac{\partial S}{\partial t} = \nabla \cdot (\mathbf{D}_S \nabla S) - J_{\mathrm{JSR}} + \frac{v_{\mathrm{SR}}}{v_{cyt}} (J_{\mathrm{pump}} - J_{\mathrm{leak}}) \qquad \text{in} \quad Q, \tag{11}$$

 $\mathbf{D}_S=\mathrm{diag}(D_S,D_S,D_S)$ is the diffusion matrix for the SR Ca^{2+} concentration . We use the bidomain approximation for cytosol and SR [20]. In this concept, both compartments occupy the same computational volume continuously with volume ratio $v_{\rm SR}/v_{\rm cyt}$. We impose homogeneous Neumann boundary conditions for the SR Ca^{2+}

$$\vec{n} \cdot \mathbf{D}_S \nabla S = 0$$
 on $\Gamma \times [0, T]$,

2.1.2. Detailed CRU model

In our computational framework, we used a previously developed model for individual CRUs [21], which is briefly summarized below. It features a spatially resolved description of the dyadic cleft with channel placement based on nanometer-scale microscopy studies [22,23] and representation of the junctional sarcoplasmic reticulum (jSR). The dyadic cleft is modeled as a cylindrical compartment with a height of 15 nm, where the RyRs at the jSR membrane are colocalized with the LCCs at the T-tubule membrane. The behavior of the CRU is mainly governed by three different dynamics: the gating of the main Ca^{2+} -channels

(1)

(LCCs and RyRs), the Ca^{2+} -profile within the dyadic cleft, and the Ca^{2+} -content-dynamics of the jSR. Each individual channel is modeled as a Markov process representing different conformal states, which may either be conductive or non-conductive. Ca^{2+} concentrations inside the dyadic cleft are computed under a quasi-steady-state assumption, which allows for efficient computations of Ca^{2+} -concentrations inside the space whenever either a channel changes state, jSR content changes, or external parameters change. The dynamics for each individual CRU are computed for a small timestep Δt , and the fluxes through the channels are averaged over this timestep and then used as source terms in the PDEs. (3) and (10).

$$J_{c}^{i} = \frac{1}{\Delta t} \left(\sum_{j=1}^{N_{RyR}^{i}} \int_{t}^{t+\Delta t} J_{RyR}^{i,j}(t) dt + \sum_{j=1}^{N_{LCC}^{i}} \int_{t}^{t+\Delta t} J_{LCC}^{i,j}(t) dt \right)$$
(12)

$$J_{\rm jSR}^i = \frac{1}{\Delta t} \left(\int_t^{t+\Delta t} \frac{c_{\rm NSR}^i - c_{\rm jSR}^i(t)}{\tau_{\rm Refill}} dt \right) \tag{13}$$

Here, $J_\chi^{i,j}$ is the current through the jth channel of type X in CRU i, N_χ^i is the number of channels of type X in CRU i, $c_{\rm NSR}^i$ is the free Ca²⁺ concentration in the sarcoplasmic reticulum at the location of the connection to the jSR compartment of the ith CRU and $c_{\rm jSR}^i$ is the Ca²⁺ concentration in the corresponding jSR compartment.

2.1.3. Membrane potential model

Our model includes two variants for computing membrane potential and non-diffusive ion concentrations. The first variant simulating rabbit cells based on a model by Mahajan et al. [19] has been presented [22,24]. Additionally, we implemented a model for rat cells, based on an adapted version of the rat electrophysiology model by Stevenson-Cocks [25]. In both cases, all Ca²⁺-related dynamics and currents in the original are replaced with the computations described above. This includes the release currents from LCCs and the sodium–calcium–exchanger (NCX), whose values are computed in our model as follows:

$$\begin{split} I_{\text{NCX}} &= \frac{V_{\text{cell}}}{|\varOmega|} \int_{\varOmega} J_{\text{NCX}} + \frac{A_{\text{cell}}}{|\partial \varOmega|} \int_{\partial \varOmega} J_{\text{NCX}}^{\text{pm}} \\ I_{\text{LCC}} &= \frac{20000}{N_{\text{CRU}}} \sum_{i=1}^{N_{\text{CRU}}} I_{\text{LCC}}^{i} \end{split}$$

2.2. Numerical approach

2.2.1. Spatial discretization and adaptivity

We denote the inner product and norm in $L^2(\Omega)$ by (\cdot,\cdot) and $|\cdot|$, respectively, and similarly the inner product and norm on $H^1(\Omega)$ are denoted by $(\cdot,\cdot)_{H^1}$ and $\|\cdot\|$. It is assumed throughout that for a constant 0 < k < K

$$k|\xi|^2 \le \xi^T D_i \xi \le K|\xi|^2$$
, for all $\xi \in \mathbb{R}^d$. (14)

The spatial discretization is based on the conforming finite element method. The variational form is obtained by multiplying the state equations by arbitrary test functions $\phi_1,\phi_2,\phi_3,\phi_4,\phi_5\in H^1(\Omega)$, and integrating over the computational domain Ω : find $c,b_s,b_m,S,B_m\in H^1(\Omega)$

$$\int_{\Omega} \frac{\partial c}{\partial t} \phi_{1} dx = -\int_{\Omega} (D_{c} \nabla c) \cdot \nabla \phi_{1} dx - \int_{\Omega} \phi_{1} J_{c}(c, b_{s}, b_{m}, S) dx$$

$$\int_{\Omega} \frac{\partial b_{s}}{\partial t} \phi_{2} dx = -\int_{\Omega} (D_{s} \nabla b_{s}) \cdot \nabla \phi_{2} dx + \int_{\Omega} \phi_{2} R_{s}(c, b_{s}) dx$$

$$\int_{\Omega} \frac{\partial b_{m}}{\partial t} \phi_{3} dx = -\int_{\Omega} (D_{m} \nabla b_{m}) \cdot \nabla \phi_{3} dx + \int_{\Omega} \phi_{3} R_{m}(c, b_{m}) dx$$

$$\int_{\Omega} \frac{\partial S}{\partial t} \phi_{4} dx = -\int_{\Omega} (D_{S} \nabla S) \cdot \nabla \phi_{4} dx + \int_{\Omega} \phi_{4} J_{s}(c, B_{s}) dx$$

$$\int_{\Omega} \frac{\partial B_{m}}{\partial t} \phi_{4} dx = -\int_{\Omega} (D_{m} \nabla B_{m}) \cdot \nabla \phi_{4} dx + \int_{\Omega} \phi_{4} H_{m}(S, B_{m}) dx$$
(15)

where $J_c(c,b_s,b_m,S)$ is the sum of the fluxes from Eq. (1) and $J_s(c,B_s)$ is the total flux from Eq. (11). Let $V_h \subset H^1(\Omega)$ be the finite-dimensional subspace of piecewise linear basis functions with respect to the spatial grid.

The approximate solutions c^h , b^h_s , b^h_m and b^h_d can be expressed in the form

$$c^{h}(t,x) = \sum_{i=1}^{N} c^{i}(t)\phi_{i}(x),$$
 (16)

$$b_s^h(t,x) = \sum_{i=1}^{N} b_s^i(t)\phi_i(x),$$
(17)

$$b_m^h(t,x) = \sum_{i=1}^{N} b_m^i(t)\phi_i(x),$$
 (18)

$$S^{h}(t,x) = \sum_{i=1}^{N} b_{d}^{i}(t)\phi_{i}(x)$$
 (19)

$$B_m^h(t,x) = \sum_{i=1}^N B_m^i(t)\phi_i(x),$$
 (20)

respectively where $\{\phi_i(x)\}_{i=1}^N$ denote the basis functions and N is the number of nodal points. We use the standard definitions of the mass matrix $M \in \mathbb{R}^{N \times N}$ whose elements are defined by $M_{kl} = \int_{\Omega} \phi_k \phi_l dx$ and the stiffness matrix $A \in \mathbb{R}^{N \times N}$ with $A_{kl} = \int_{\Omega} \nabla \phi_k \nabla \phi_l dx$. Finally, the above-mentioned semi-discretization in space results in the ordinary differential equation system in block matrix form

$$\mathbf{M}\frac{\partial \mathbf{u}}{\partial t} = -\mathbf{A}\mathbf{u} + \mathbf{F}(\mathbf{u}) \tag{21}$$

where $\mathbf{u} = (\mathbf{c}, \mathbf{b}_{\mathbf{s}}, \mathbf{b}_{\mathbf{m}}, \mathbf{S}, \mathbf{B}_{\mathbf{m}})^T$ and $\mathbf{F}(\mathbf{u})$ is a vector based on the reaction terms from the state equations Eq. (1), (2) and (11). The global mass and stiffness matrices are $\mathbf{M} = \operatorname{diag}(M, M, M, M, M)$ and $\mathbf{A} = \operatorname{diag}(A, A, A, A, A)$.

In our computational framework, the adaptive mesh refinement (AMR) technique is built upon gradient-type error estimators, specifically the Z^2 error indicator introduced by Zienkiewicz and Zhu [16]. To provide a concise overview, we describe the essential components of the ZZ error indicator. Let W_h be the space of all piecewise linear vector fields, and define the subspace $X_h := W_h \cap C(\Omega, \mathbb{R}^3)$, where $C(\Omega, \mathbb{R}^3)$ represents the space of continuous vector fields on the domain Q.

Let v and v_h denote the exact solution and the numerical solution, respectively, of the state equations (Eqs. (1)–(11)) and the semi-discretized state equations (Eq. (15)) at a fixed time t. The error between the numerical and exact solutions can be estimated using the L^2 norm of the difference between the gradients, $\|Gv_h - \nabla v_h\|_{L^2(T)}$, where Gv_h is a computed approximation of the gradient ∇v_h . This approximation is obtained by averaging the local gradients $\nabla v_h|_T(\mathbf{x}_i)$ over neighboring elements, as described by Zienkiewicz and Zhu [16]. Specifically, the gradient approximation Gv_h at a point \mathbf{x}_i is computed as follows:

$$Gv_h(\mathbf{x}_i) = \sum_{T \in \mathcal{D}} \frac{|T|}{|D_{\mathbf{x}}|} \nabla v_{h|T}(\mathbf{x}_i). \tag{22}$$

where D_x represents the union of tetrahedra sharing the vertex \mathbf{x}_i , and |T| and $|D_x|$ are the volumes of the tetrahedron T and the region D_x , respectively. This local averaging approach allows for a more robust and reliable estimation of the gradient.

The local error indicator $\eta_{Z,T}$ at an element T is defined as the L^2 norm of the difference between the averaged gradient Gv_h and the exact gradient ∇v_h :

$$\eta_{Z,T} := \|Gv_h - \nabla v_h\|_{L^2(T)} , \qquad (23)$$

which quantifies the error within the element T. The global error indicator η_Z is then computed by summing the squared local error

indicators over all elements in the mesh \mathcal{T}_h and taking the square root:

$$\eta_Z := \left\{ \sum_{T \in \mathcal{T}_h} \eta_{Z,T}^2 \right\}^{1/2} . \tag{24}$$

This global error indicator provides a measure of the overall approximation accuracy across the entire computational domain. The Z^2 indicator $\eta_{Z,T}$ serves as an estimate for the error in the gradient of the solution, specifically $\|\nabla u_h^t(\cdot,t_i) - \nabla u^t(\cdot,t_i)\|_{L^2(T)}$, where $u_h^t(\cdot,t_i)$ and $u^t(\cdot,t_i)$ are the numerical and exact solutions at time t_i , respectively. For a more detailed discussion of these error indicators, refer to Verfürth [26].

2.2.2. Temporal discretization and adaptivity

In this section, we discuss the time discretization approach to solve the semi-discretized equations Eqs. (21). For the time discretization, we use linearly implicit Runge-Kutta methods, specifically Rosenbrocktype methods. This class of methods avoids solving the nonlinear system and replaces it with a sequence of linear ones. Moreover, a straightforward embedding technique is applied to estimate the error introduced by the time discretization, which is then used to compute adaptive time steps. The semi-discretized equations can be expressed in the following general coupled formulation of ODEs,

$$\mathbf{M}\frac{d\mathbf{u}}{dt} = \mathbf{F}(\mathbf{u}), \qquad \mathbf{u}(t^0) = \mathbf{u}^0. \tag{25}$$

We further set $\tau^i = t^{i+1} - t^i$ and denote by \mathbf{u}^i the numerical solution at

For brevity, an s-stage Rosenbrock method, see [27] for details, of order p with embedding of order $\hat{p} \neq p$ has the form,

$$\left(\frac{1}{\tau^{i}\gamma}\mathbf{M} - \mathbf{J}\right)\mathbf{k}_{j} = \mathbf{F}\left(t^{i} + \tau^{i}\alpha_{j}, \mathbf{u}^{i} + \sum_{l=1}^{j-1} a_{jl}\mathbf{k}_{l}\right) - \mathbf{M}\sum_{l=1}^{j-1} \frac{c_{lj}}{\tau^{i}}\mathbf{k}_{l}, \quad j = 1, \dots, s,$$
(26)

$$\mathbf{u}^{i+1} = \mathbf{u}^i + \sum_{l=1}^s m_l \mathbf{k}_l \,, \tag{27}$$

$$\hat{\mathbf{u}}^{i+1} = \mathbf{u}^i + \sum_{l=1}^s \hat{m}_l \mathbf{k}_l. \tag{28}$$

The coefficients $\gamma, \alpha_i, a_{il}, c_{il}, m_l$, and \hat{m}_l are chosen in such a way that certain consistency order conditions are fulfilled to obtain a sufficiently high convergence order. For the construction of the Jacobian matrix J. we used exact derivatives of the vector $\mathbf{F}(\mathbf{u})$. A second solution $\hat{\mathbf{u}}^{i+1}$ of lower order \hat{p} is constructed to estimate the error part to predict the future time step τ^{i+1} , where we assume that $p > \hat{p}$. Specifically, we use the ROWDA method, see [27], which is a 3(2) order method with three internal stages. The parameters appearing in Eqs. (26)-(28) can be found in [27]. We tested this method previously and found it to be highly efficient [7,28]. ROWDA was chosen based on those results because of its computational efficiency and to ensure stability and accuracy for the present system. In our numerical computations, a new time step τ_{i+1} is computed based on the idea of Gustafsson et al. [29].

We employed a BiCGSTAB method with block Jacobi preconditioning to solve the system of equations that appears after the time discretization of (26) at each internal stage of the ROWDA method.

2.2.3. Parallel implementation

In our numerical experiments, we implemented the parallel spacetime dynamic adaptivity code using the public domain software package DUNE [17] and Dune-PDELab [30]. Our implementation employs a non-overlapping decomposition for mesh partitioning. Briefly, the computational domain Ω is divided into several sub-domains Ω_n , where n is the number of computing cores, and each subdomain is assigned to one computing core. Although domain decomposition techniques are beyond the scope of this work, further details on the parallel implementation can be found in [31]. In our implementation, we use the ALUGrid interface [32] for grid construction and the METIS graph partitioning software [33] for dynamic load balancing of the grid. For this purpose, we utilize the serial k-way multilevel graph partitioning algorithm, which facilitates the partitioning of the computational mesh at each time step, ensuring efficient load balancing across the computational

Parallel and space-time adaptivity approach. Let us assume that the simulation begins with a relatively coarse mesh, denoted as L_0 , which serves as the central mesh at the root level of the hierarchical system. Finer mesh levels, L_i for i > 0, are recursively generated from the coarser level \mathcal{L}_{i-1} by refining the computational grid. In our numerical experiments, the spatial grid refinement tolerance is set to Tol_x = 10^{-3} . The Z^2 error estimator is invoked at every proposed time step, following the solution of the deterministic-stochastic solver. The grid is adapted if either the spatial error exceeds the prescribed tolerance Tol_x or if the error falls below $0.001 \cdot Tol_x$. Once the grid is adapted, the solution is updated on the new grid using linear interpolation or restriction. To ensure proper load balancing, the grid is redistributed, and the solution data is reallocated accordingly.

After the solution data is redistributed to the newly adjusted grids, the time discretization step is applied to compute the new solution. If the error at the suggested time step, computed using a simple embedding time-stepping technique, is less than the prescribed tolerance, the proposed step size is accepted. Otherwise, the time step is reduced according to the time step controller. This process is repeated until an appropriate step size is determined. In this way, our numerical framework simultaneously applies both dynamic mesh refinement and time step control, ensuring efficient and accurate simulations. The complete parallel space-time adaptivity strategy for simulating sparks is detailed in Algorithm A1.

3. Results

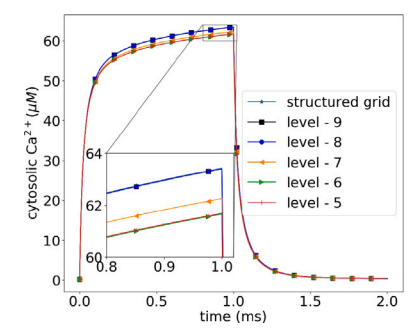
In this section, first, we demonstrate the numerical convergence tests based on the space-time adaptivity grids and fixed finer grids for the single CRU setup and then for one complete action potential simulation on reasonable geometries.

3.1. Adaptivity versus non-adaptivity

Results with one CRU

In this section, we examine the numerical convergence of solutions for a single CRU setup. This test case serves as a foundation for determining the grid sizes used in subsequent simulations. The computational domain (Ω) for this simulation is a cube $[0,2]\times[0,2]\times[0,2]$, with a volume of 8 μ m³. The CRU is positioned in the center of the domain, with a fixed radius of $0.144853 \mu m$. The number of LCC and RyR channels is set to 4 and 23, respectively, with constant channel fluxes applied when the channels open. These fluxes are derived from a stochastic simulation conducted on a similar setup. The total simulation time is 2 ms. The CRU opens deterministically during the first millisecond and remains open until 1 millisecond, after which it closes until the end of the 2-millisecond simulation period. The coarsest grid in the simulation consists of $16 \times 16 \times 16$ elements, referred to as the level-0 grid, corresponding to the smallest edge size of 216 nm.

The convergence of the cytosolic solution Ca²⁺ over time is illustrated on the left side of Fig. 3, while its convergence with respect to the distance from the CRU center is shown on the right side of the same figure. These results are presented for different maximum levels of mesh refinement. The reference solution used for comparison is computed on a structured uniform grid with dimensions $256 \times 256 \times 256$, corresponding to the smallest edge size of 7.8 nm. It is evident that the solutions computed on the level-8 and level-9 grids closely match



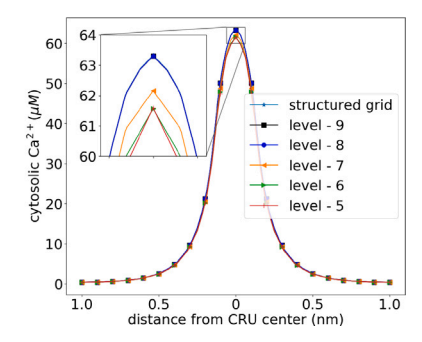


Fig. 3. Convergence of solutions for different spatial grid refinement levels. Shown are Ca^{2+} concentrations at a reference point at the center of the computational domain in the left panel and along a line through the center of the domain at 1 ms simulation time in the right panel. The reference solution (labeled structured grid) and a range of solutions obtained by limiting the maximum grid refinement to the given levels are shown. Note that the lines for refinement levels eight and nine are identical to the reference solution. The solution has converged.

Table 2Accuracy in space adaptivity. The maximum relative errors for the different diffusive ion species in the model are shown, depending on the maximum allowed grid refinement.

Mesh size	Min edge	Relative err	Relative errors				
	size (in nm)	err _c	err_{b_m}	err_{b_s}	err_S	err_{B_m}	
level - 5	54.1	0.6613	0.1011	0.4123	0.8613	0.1862	
level - 6	27.0	0.4106	0.0617	0.2506	0.5809	0.0899	
level - 7	15.6	0.1001	0.0108	0.0883	0.2003	0.0354	
level - 8	13.1	0.0094	0.0021	0.0090	0.0302	0.0045	
level - 9	7.6	0.0010	0.0003	0.0011	0.0071	0.0009	

the results obtained from the finer-structured, uniform grid solution in both cases. This alignment indicates that the numerical solution has converged to the reference solution as the mesh refinement increases.

In the following discussion, we evaluate the accuracy of numerical solutions in the context of spatial grid adaptivity by comparing them with the solution obtained from a fine-structured grid, which has a minimum edge length of 7.8 nm. The relative error of the finite element (FE) solutions in the L^2 norm is calculated as follows.

$$err_{X}(t) = \frac{\left\| X(.,t) - Y_{f}(.,t) \right\|_{L^{2}(\Omega)}}{\left\| Y_{f}(.,t) \right\|_{L^{2}(\Omega)}}.$$
 (29)

Let X(.,t) represent the spatially distributed FE solution of the state variables at the simulation time instance t=1ms, which corresponds to the point when the CRU opens. The solution obtained on the finer structured grid at a given level is denoted by $Y_f(.,t)$. Since the exact solution is unknown, this finer grid solution is treated as the reference solution. It is computed using a fixed small time step size, $\tau=0.001$ ms. The simulation employs adaptive time steps, enabling the computation of the solution on spatially adaptive grids. The relative errors for the state variables are presented in Table 2. The second column of the table indicates the minimum edge length of the elements in the level's mesh computations. From the table, we observe that the relative errors for the level-7 to level-9 grid computations are significantly smaller compared to those for the computations on coarser grids, highlighting the improved accuracy with finer meshes.

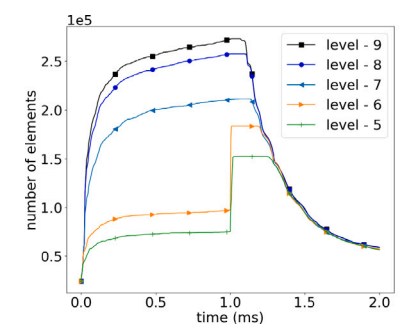
The number of elements, nodes, and adaptive time steps involved in the simulation of the single CRU setup is illustrated in Fig. 4. For the setup with a maximum of 9 levels of mesh refinement, the number of elements and nodes increases to 273,260 and 49,053, respectively, at the simulation time of 1 millisecond. In contrast, when using a maximum of 8 levels of mesh refinement, the number of elements and nodes reaches 257,854 and 46,538, respectively, at the same time point. At the 1 ms mark, the space–time algorithm achieves the maximum number of elements, with the largest time step being 0.1 ms. After the CRU has been open for the first millisecond, the simulation switches to a closed state, and the space adaptivity algorithm gradually reduces the number of refined elements, returning the computational grid to the coarsest

mesh level. This approach ensures that computational resources are efficiently utilized, focusing on refinement when the system is more dynamic and less so when it is steady. The computational mesh at various times during the simulation is shown in Fig. 5, highlighting the transition of mesh refinement over time, as dictated by the adaptive strategy.

Next, we analyze the CPU times for the deterministic opening of a single CRU setup. The absolute computational times on a single core for different mesh levels are provided in Table 3. From these results, we observe that assembling the matrices consumes the largest portion of the computational time, surpassing other components of the simulation. Additionally, the grid adaptivity process, which includes the error estimator and the transfer of solutions between finer and coarser grid levels, also contributes significantly to the overall CPU time. Adaptive time steps, which allow for the computation of the solution on structured grid simulations, further influence the computational time. Despite these factors, the space-time adaptive simulations are notably faster compared to simulations using fixed uniform grids. To quantify this, we calculate the speedup factor, which compares the time taken by the space-time adaptive simulations to that of the fixed structured grid simulations. The speedup factor is found to be 6.91 for the level-8 setup and 6.09 for the level-9 setup.

3.2. Action potential simulation

For the action potential simulations, the computational domain is consists of a quarter z-disc with dimensions of $10\times10\times2\,\mu\mathrm{m}^3$. The coarse grid consists of 1,200,000 tetrahedral elements and 214,221 nodes structured as a $100\times100\times20$ element grid. Here, we set the maximum grid refinement level to 6, ensuring that the refined grid reduces the element's minimum edge size to approximately 6 nm. The simulations were run on a Padmanabha cluster, IISER Thiruvananthapuram, India, which consists of 88 computing nodes. Each node is configured with two Intel Xeon Gold 6132 CPUs, each with 14 cores (28 cores per node in total), running at 2.60 GHz, and equipped with 128 GB of RAM. Various time-stepping strategies for independent sequences of channel events have been discussed in Chamakuri et al. [15], and we apply the same strategies in our space–time adaptive simulations. Three action



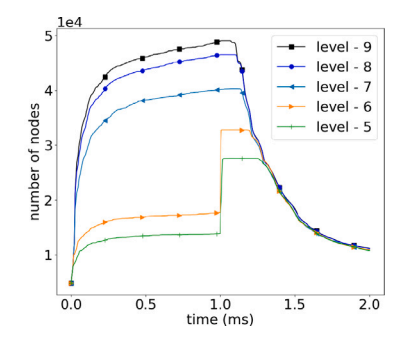


Fig. 4. The number of elements and nodes over the simulation time for a single CRU setup computation. The reference simulation used more than $1.6 \cdot 10^7$ elements and a similar amount of nodes and can therefore not be included in the graph.

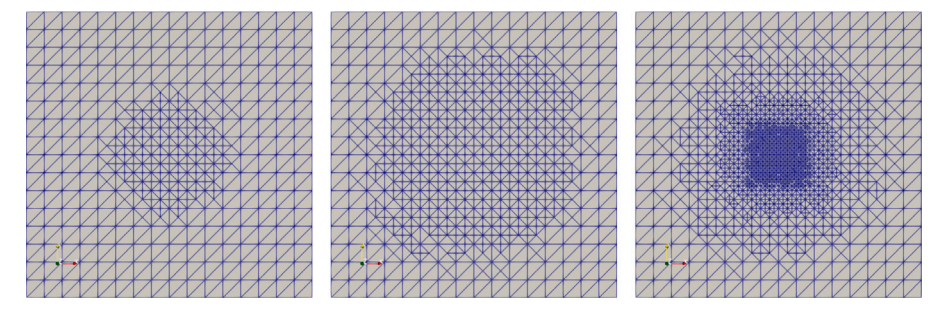


Fig. 5. Computational mesh at different time instances t = 0.0002, 0.002 and 0.998 during the simulation of a single CRU setup illustrating the evolution and refinement of the grid.

Table 3The absolute CPU timings and speedup factors for the simulation of the deterministically opening of a single CRU setup at different mesh refinement levels.

Mesh size	CPU times (in		Speedup		
	Assembly	Linear solver	Grid adaptivity	Total	
level - 5	275.74	82.90	140.60	533.27	15.78
level - 6	327.60	106.45	174.26	642.45	13.01
level - 7	522.76	191.34	300.16	1043.65	8.06
level - 8	599.56	240.92	365.62	1218.01	6.91
level - 9	671.14	278.67	421.04	1390.21	6.05
Structured grid	5943.64	2445.51	-	8418.14	1

potential time courses are illustrated in Fig. 7(a). Initially, there is a rapid upstroke from the resting potential of approximately -85 mV to a peak of about 40 mV. Following this, the membrane potential enters a plateau phase before repolarizing back to the resting potential at around 140 ms. During the rapid upstroke of the action potentials, many CRUs (calcium release units) open, and the mesh within the cluster area and its surroundings undergo refinement. This refinement leads to the maximum number of elements being reported during this phase. As the action potential progresses into the repolarization phase, fewer CRUs are activated, resulting in a coarsening of most elements. This results in reduced computational demand, as only a small number of elements are needed during the repolarization phase, where a few channels open randomly within the clusters, as shown clearly in Fig. 7(b). This refinement and coarsening strategy significantly reduces the CPU time required to solve the hybrid simulations, particularly during the less active phases. The maximum number of elements recorded during the simulations occurred at 40.90 ms of simulation time, reaching a total of 4,396,710 elements. A similar reduction in the number of elements was observed during the other action potential upstroke phases, further demonstrating the efficiency of the space-time adaptive approach in optimizing computational resources (see Fig. 6).

In the context of the parallel implementation of the space-time adaptive approach across 168 CPU cores, the total computational

time required to complete the three action potential simulations is 37.41 h. On the other hand, when utilizing a structured grid of size $600 \times 600 \times 80$, the computation across the same 168 cores takes significantly longer, requiring a total of 79.68 h. This represents a time increase, making the structured grid simulation 2.13 times slower compared to the adaptive spatial simulation. The difference in computational efficiency highlights the increased performance of the space-time adaptive approach when implemented in parallel on a large number of cores. The overall computational process was divided into several key stages, each requiring specific amounts of time. The assembly of the matrices was completed in 7.04 h. Following this, the solution of the linear systems, a critical step for obtaining the desired results, took 16.32 h. Additionally, the ZZ error estimator and guiding the grid adaptivity process took 9.56 h to execute. Lastly, the dynamic load balancing of the grid, which ensures an even distribution of computational tasks across processors, required 2.61 h.

Parallel performance results

For this benchmark simulation, the total duration of the simulation is 2 ms. During the first millisecond, the CRU opens in a deterministic manner and remains open until the 1-millisecond mark. Afterward, it closes and remains shut for the remainder of the 2-millisecond

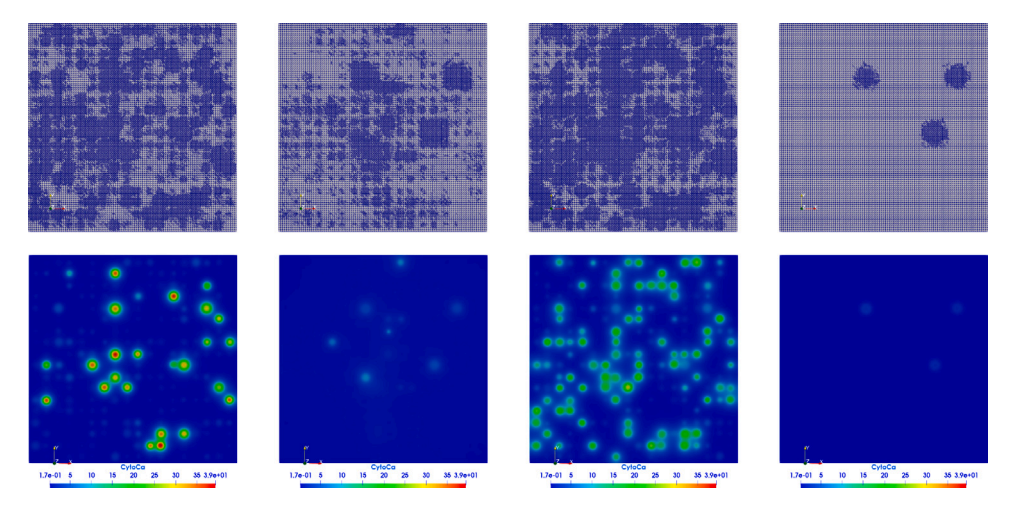


Fig. 6. The space–time adaptive computational grid and the corresponding contour plots illustrating the spatial distribution of cytosolic Ca^{2+} concentration during a single full Z-disc action potential simulation at the time points t = 9.10, 174.10, 369.10, and 674.10 ms. Results are shown on the mid-plane ($z = 1 \mu m$), corresponding to the full xy-plane of the domain with a size of 10 μm × 10 μm.

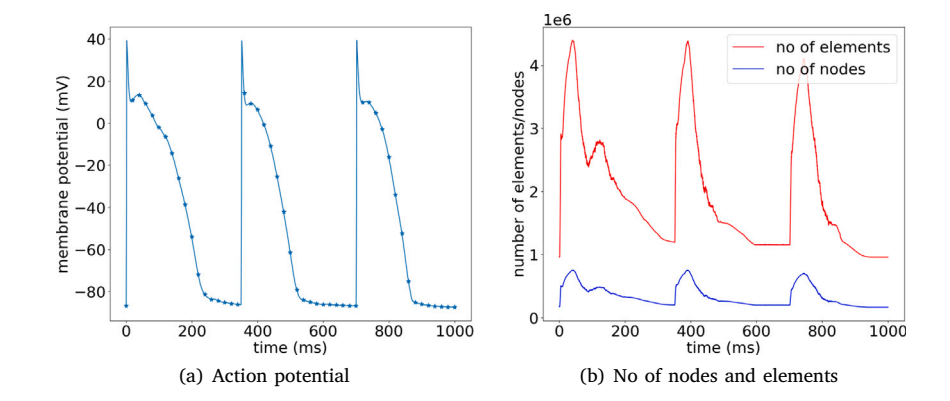


Fig. 7. Space—time adaptive simulation of a single full Z-disc action potential over the entire time period. The left panel depicts action potential dynamics, and the right panel shows the number of computational elements and nodes used, illustrating the dynamic adjustment of mesh resolution in response to changing physiological conditions.

simulation period, following the same behavior as observed in the convergence tests of the single CRU setup. For these deterministic simulations, the fluxes are derived from a stochastic simulation conducted on a similar setup. The coarse grid used in the simulation comprises 1,200,000 tetrahedral elements and 214,221 nodes, arranged in a grid with dimensions of $100\times100\times20$ elements. This benchmark simulation illustrates the strong scaling properties of both the Jacobian matrix assembly and the overall simulation time. The results are presented in Fig. 8. Notably, we observed that the maximum number of elements reported during the simulations occurred at the 1-millisecond point, reaching a total of 5,831,664 elements.

3.3. Spark simulation

Investigating spontaneous Ca²⁺ release events (called sparks) is a core feature of our model. Sparks and their formation, termination, and morphology are of interest in cardiac research and modeling [34, 35]. They allow insights into the core mechanics of CICR in cardiac myocytes and are experimentally comparable and easy to observe and measure as opposed to single-channel currents. The methods described in this paper enable the simulation of sparks at a timescale and compute expense that makes both long-term as well as collections of a large variety of shorter simulations, such as for parameter scans, viable. The stochastic nature of sparks and their low frequency (even at pathologically increased rates) necessitate either long simulated timescales or

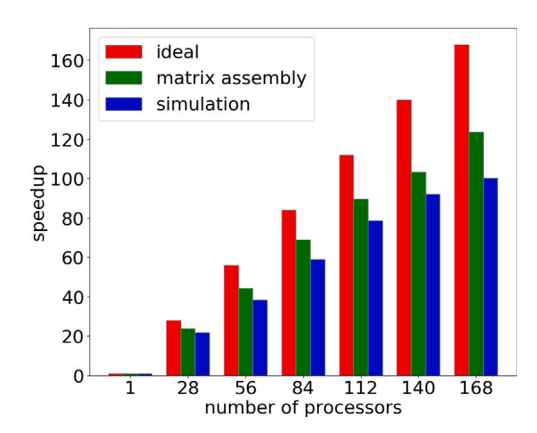
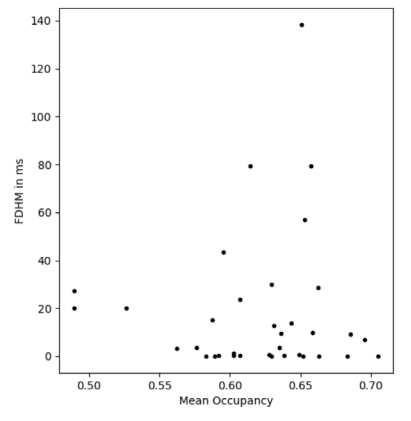


Fig. 8. Parallel speedup for up to 168 cores.

large simulated areas. Both are significant cost factors, either in time or memory. Using local space–time adaptivity, we can run simulations for varied parameter sets on an efficient time scale. Our results with these new methods introduced here are consistent with previous results (see Fig. 9), but are computed at a fraction of the time (see Table 4).



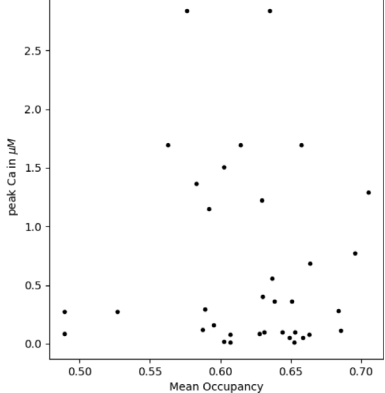


Fig. 9. Relating mean occupancies to spark morphological characteristics yields results consistent with prior research. Mean occupancy characterizes RyR cluster structure (compare Cosi et al. [22], also for a complete definition of the terms).

Table 4The absolute CPU timings and speedup factors for the simulation of a quarter Z-disc setup with or without space–time adaptivity.

Mesh-size	Total time	Speedup	
level - 6	14341 s	16.07	
Structured grid	230 389 s	1	

These simulations were conducted on the same machine with a 64-core AMD Threadripper PRO 5995WX CPU with 512 GB RAM. Their domain was a quarter z-disc of $10\times10\times2~\mu\text{m}^3$ with a rectangular structured grid of $600\times600\times80$ nodes. The coarsest level of the space–time adaptive grid was $100\times100\times40$. More detailed comparisons of spark simulations in our model with experimental results are presented in Neubert et al. [36]

4. Discussion

We have demonstrated the efficiency of our simulation techniques for multi-scale simulations of Ca²⁺ dynamics in ventricular cardiomy-ocytes. Speedups by a factor of 16 enable simulations over time courses and scopes that would not be feasible without space–time adaptivity.

This speed of simulations opens the door to further model development responding to current medical research. Structural aspects and, consequently, the importance of gradients of cytosolic and dyadic Ca²⁺ are the subject of ongoing discussions, for example, in relation to heart failure with preserved ejection fraction (HFpEF). Animal models of HFpEF exhibit insufficient relaxation in diastole and the NCX has been identified as a potential drug target for ameliorating myocyte relaxation [37,38]. The NCX has been found to be colocalized with CRUs in most species, including rat [39] and rabbit [40], but some microscopy studies seem to contradict this [41]. Modeling suggests that the arrhythmogenic potential of NCX in conjunction with delayed after-depolarizations is stronger with NCX inside the dyadic space compared to NCX being close to CRUs [42]. Sub-dyadic modeling showed substantial concentration gradients inside dyadic clefts [21, 24,43]. Hence, these structural details are relevant. Modeling them requires solving the reaction-diffusion equations on the length scale of RyR distances inside the cleft and of CRU size in the vicinity of CRUs. Investigating the effect of NCX localization on action potentials and myocyte relaxation requires simulating cell behavior at the same time. The space-time adaptivity established in this study allows for those multi-scale simulations and enables modeling to investigate these disease-related questions.

CRediT authorship contribution statement

Wilhelm Neubert: Writing – review & editing, Writing – original draft, Visualization, Validation, Software, Methodology, Investigation, Formal analysis, Data curation, Conceptualization. Martin Falcke: Writing – review & editing, Visualization, Validation, Resources, Project administration, Methodology, Investigation, Funding acquisition, Formal analysis, Conceptualization. Nagaiah Chamakuri: Writing – review & editing, Writing – original draft, Visualization, Validation, Software, Resources, Methodology, Investigation, Formal analysis, Conceptualization.

Ethics approval

This study is purely theoretical and computational in nature. It does not involve any experiments on human participants, animals, or the use of identifiable personal data. Therefore, no ethical approval or informed consent is required.

Declaration of Generative AI and AI-assisted technologies in the writing process

During the preparation of this work the authors used ChatGPT 40 in order to refine the language and improve the clarity of this manuscript. After using this tool/service, the authors reviewed and edited the content as needed and take full responsibility for the content of the published article.

Declaration of competing interest

The authors declare the following financial interests/personal relationships which may be considered as potential competing interests: Wilhelm Neubert reports financial support was provided by German Research Foundation. Nagaiah Chamakuri reports equipment, drugs, or supplies was provided by Indian Institute of Science Education and Research Thiruvananthapuram. If there are other authors, they declare that they have no known competing financial interests or personal relationships that could have appeared to influence the work reported in this paper.

Acknowledgments

W.N. has been supported by DFG, Germany grant FA 350/17-1 to M.F. We acknowledge the support for high-performance computing time at the Padmanabha cluster, IISER Thiruvananthapuram, India. Since this is a purely computational study, no ethics approvals were required. The authors declare no competing interests.

Table 5A full list of all named parameters in this paper, including their values. All other parameter values are as they are listed in [15,24]. Species-specific parameters for rat membrane potential dynamics are taken from [25].

Parameter	Description	Value
D_c	Diffusion constant for unbound Ca ²⁺ in the cytosol	0.220 μm ² /ms
D_m	Diffusion constant for Ca ²⁺ bound mobile buffers in the cytosol	$0.04 \ \mu m^2/ms$
D_s	Diffusion constant for Ca ²⁺ bound immobile buffers in the cytosol	0 μm²/ms
D_f	Diffusion constant for Ca2+ bound fluorescent buffer in the cytosol	$0.033 \ \mu m^2/ms$
b_m^{tot}	Total concentration of mobile Ca ²⁺ buffer in the cytosol	25.0 μM
b_s^{tot}	Total concentration of immobile Ca ²⁺ buffer in the cytosol	70 μ M
b_m^{tot} b_s^{tot} b_f^{tot}	Total concentration of fluorescent Ca ²⁺ buffer in the cytosol	25 μM
V_P^{\max}	SERCA maximum pump speed	1. μM/ms
K_P	SERCA half maximum concentration	0.2 µM
$v_{ m SR}$	Volume ratio of SR compartment	0.1
$v_{ m cyt}$	Volume ratio of cytosolic compartment	0.9
K_d	Dissociation constant of the fluorescent buffer	345 nM
$ au_{ m Refill}$	jSR Refill flux time constant	3.9 ms
$V_{ m cell}$	Total volume of a rat cardiomyocyte	$2.58 \times 10^4 \ \mu m^3$
$A_{ m cell}$	Total surface area of a rat cardiomyocyte	7290 μm ²

Appendix A. Algorithm

1. Initialization

• Set $\mathbf{u}_{old} = \mathbf{u}_0$, $t_{old} = 0$ and $\Delta t > 0$. Here the solution \mathbf{u} represents all unknown quantities from the state equations.

2. Stochastic CRU dynamics

- Compute the event times (t_{old} + Δt_i) ∈ [t_{old}, t_{old} + Δt] for all CRUs i = 1,..., N_c by applying the single CRU dynamics as described in [22,24].
- Compute average RyR and LCC fluxes, jSR Ca^{2+} content and individual Channel States at time $t_{old} + \Delta t$

3. Update Bulk Calcium Cycling Dynamics

- Compute new solution u_{new} based on the available old solution u_{old} the time step Δt and the fluxes from the CRUs averaged over the timestep Δt.
- If the time step integrator (Rosenbrock type) of the discretized PDE system rejects the current time step, then determine the new time step Δt_{new} according to local error criterion of the time step integrator and assign $\Delta t := \Delta t_{new}$ and go to 2.

4. Update membrane potential dynamics

• Compute the new solution of V_{new} based on the \mathbf{u}_{new} and the current LCC, RyR and NCX fluxes.

5. Adapt the grid at time Δt

- Apply the Z^2 error estimator to find the error at the computational mesh and adapt the grid accordingly.
- Call re-load balance of the grid using ALUGrid spacefilling curve approach package if it has changed and then assemble the matrices and vectors accordingly.
- 6. Set $t_{old} := t_{old} + \tau_{stoc}$ and go to 2.

Appendix B. Parameters

See Table 5.

Appendix C. Supplementary data

Supplementary material related to this article can be found online at https://doi.org/10.1016/j.cmpb.2025.109154.

References

- J.A.E. Alvarez, M.S. Jafri, A. Ullah, Local control model of a human ventricular myocyte: An exploration of frequency-dependent changes and calcium sparks, Biomolecules 13 (8) (2023).
- [2] W. Chen, J.A. Wasserstrom, Y. Shiferaw, Role of coupled gating between cardiac ryanodine receptors in the genesis of triggered arrhythmias, Am. J. Physiol-Heart Circ. Physiol. 297 (1) (2009) H171–H180, PMID: 19429830.
- [3] H. Cheng, W.J. Lederer, Calcium sparks, Physiol. Rev. 88 (4) (2008) 1491–1545, PMID: 18923188.
- [4] M.M. Maleckar, A.G. Edwards, W.E. Louch, G.T. Lines, Studying dyadic structure-function relationships: a review of current modeling approaches and new insights into Ca2+ (mis) handling, Clin. Med. Insights: Cardiol. 11 (2017) 1179546817698602.
- [5] E.M. Cherry, H.S. Greenside, C.S. Henriquez, A space-time adaptive method for simulating complex cardiac dynamics, Phys. Rev. Lett. 84 (6) (2000) 1343–1346.
- [6] P.C. Franzone, P. Deuflhard, B. Erdmann, J. Lang, L.F. Pavarino, Adaptivity in space and time for reaction-diffusion systems in electrocardiology, SIAM J. Numer. Anal. 28 (3) (2006) 942–962.
- [7] C. Nagaiah, S. Rüdiger, G. Warnecke, M. Falcke, Adaptive numerical solution of intracellular calcium dynamics using domain decomposition methods, Appl. Numer. Math. 58 (11) (2008) 1658–1674.
- [8] N. Chamakuri, K. Kunisch, Higher order optimization and adaptive numerical solution for optimal control of monodomain equations in cardiac electrophysiology, Appl. Numer. Math. 61 (2011) 53–65.
- [9] J.A. Trangenstein, C. Kim, Operator splitting and adaptive mesh refinement for the Luo-Rudy I model, J. Comput. Phys. 196 (2) (2004) 645–679.
- [10] W. Ying, A Multilevel Adaptive Approach for Computational Cardiology (Ph.D. thesis), Duke University, 2005.
- [11] Y. Belhamadia, A. Fortin, Y. Bourgault, On the performance of anisotropic mesh adaptation for scroll wave turbulence dynamics in reaction-diffusion systems, J. Comput. Appl. Math. 271 (2014) 233–246.
- [12] D. Krause, T. Dickopf, M. Potse, R. Krause, Towards a large-scale scalable adaptive heart model using shallow tree meshes, J. Comput. Phys. 298 (2015) 70-04
- [13] J. Southern, G. Gorman, M. Piggott, P. Farrell, Parallel anisotropic mesh adaptivity with dynamic load balancing for cardiac electrophysiology, J. Comput. Sci. 3 (1) (2012) 8–16.
- [14] C. Nagaiah, S. Rüdiger, G. Warnecke, M. Falcke, Adaptive space and time numerical simulation of reaction-diffusion models for intracellular calcium dynamics, Appl. Math. Comput. 218 (20) (2012) 10194–10210.
- [15] N. Chamakuri, W. Neubert, S. Gilbert, J. Vierheller, G. Warnecke, M. Falcke, Multiscale modeling and numerical simulation of calcium cycling in cardiac myocytes, Multiscale Model. Simul. 16 (3) (2018) 1115–1145.
- [16] O.C. Zienkiewicz, J.Z. Zhu, A simple error estimator and adaptive procedure for practical engineering analysis, Int. J. Num. Meth. Eng 24 (1987) 337–357.
- [17] P. Bastian, M. Blatt, A. Dedner, C. Engwer, R. Klöfkorn, R. Kornhuber, M. Ohlberger, O. Sander, A generic grid interface for parallel and adaptive scientific computing. Part II: implementation and tests in DUNE, Computing 82 (2) (2008) 121–138.
- [18] A. Takahashi, P. Camacho, J.D. Lechleiter, B. Herman, Measurement of intracellular calcium, Physiol. Rev. 79 (4) (1999) 1089–1125.
- [19] A. Mahajan, Y. Shiferaw, D. Sato, A. Baher, R. Olcese, L.-H. Xie, M.-J. Yang, P.-S. Chen, J.G. Restrepo, A. Karma, A. Garfinkel, Z. Qu, J.N. Weiss, A rabbit ventricular action potential model replicating cardiac dynamics at rapid heart rates, Biophys. J. 94 (2) (2008) 392–410.
- [20] J. Keener, J. Sneyd, Mathematical Physiology I: Cellular Physiology, second ed. Springer, 2009.

- [21] T. Schendel, R. Thul, J. Sneyd, M. Falcke, How does the ryanodine receptor in the ventricular myocyte wake up - by a single or by multiple open L-type Ca²⁺ channels? Eur. Biophys. J. 41 (2012) 27–39.
- [22] F.G. Cosi, W. Giese, W. Neubert, S. Luther, U. Parlitz, M. Falcke, Multiscale modeling of dyadic structure-function relation in ventricular cardiac myocytes, Biophys. J. 117 (2019) 2409–2419.
- [23] I. Jayasinghe, A.H. Clowsley, R. Lin, T. Lutz, C. Harrison, E. Green, D. Baddeley, L. Di Michele, C. Soeller, True molecular scale visualization of variable clustering properties of ryanodine receptors, Cell Rep. 22 (2) (2018) 557–567.
- [24] J. Vierheller, W. Neubert, M. Falcke, S. Gilbert, N. Chamakuri, A multiscale computational model of spatially resolved calcium cycling in cardiac myocytes: from detailed cleft dynamics to the whole cell concentration profiles, Front. Physiol. 6 (2015) 255.
- [25] H. Stevenson-Cocks, Biophysical Modelling of Rat Cardiac Electrophysiology and Calcium Handling (Ph.D. thesis), The University of Leeds, 2019.
- [26] R. Verfürth, A Review of A Posteriori Error Estimation and Adaptive Mesh-Refinement Techniques, 1996,
- [27] J. Lang, Adaptive multilevel solution of nonlinear parabolic PDE systems, in: Lecture Notes in Computational Science and Engineering, vol. 16, Springer-Verlag, Berlin. 2001.
- [28] C. Nagaiah, S. Rüdiger, G. Warnecke, M. Falcke, Parallel numerical solution of intracellular calcium dynamics, in: U. Langer, M. Discacciati, D. Keyes, O. Widlund, W. Zulehner (Eds.), Domain Decomposition Methods in Science and Engineering XVII, in: Lecture Notes in Computational Science and Engineering, vol. 60, Heidelberg, 2008, pp. 155–164.
- [29] K. Gustafsson, M. Lundh, G. Söderlind, A PI stepsize control for the numerical solution of ordinary differential equations, BIT 28 (2) (1988) 270–287.
- [30] P. Bastian, F. Heimann, S. Marnach, Generic implementation of finite element methods in the distributed and unified numerics environment (DUNE), Kybernetika 46 (2) (2010) 294–315.
- [31] A. Quarteroni, A. Valli, Domain Decomposition Methods for Partial Differential Equations, Oxford University Press, Oxford, 1999.
- [32] M. Alkämper, A. Dedner, R. Klöfkorn, M. Nolte, The DUNE-ALUGrid module, Arch. Numer. Softw. 4 (1) (2016) 1–28.

- [33] G. Karypis, V. Kumar, A fast and high quality multilevel scheme for partitioning irregular graphs, SIAM J. Sci. Comput. 20 (1) (1998) 359–392.
- [34] M. Lindner, T. Böhle, D.J. Beuckelmann, Ca2+ handling in heart failure=a review focusing on Ca2+ sparks, Basic Res. Cardiol. 97 (1) (2002).
- [35] E.D. Fowler, N. Wang, M. Hezzell, G. Chanoit, J.C. Hancox, M.B. Cannell, Arrythomgenic late Ca2+ sparks in failing heart cells and their control by action potential configuration, Proc. Natl. Acad. Sci. USA 117 (5) (2020) 2687–2692.
- [36] W. Neubert, J. Hüttemeister, P. Sander, N. Chamakuri, F. Hohendanner, M. Falcke, F. Heinzel, When NCX switches sides: Experimental and computational insights into Ca²⁺ regulation in the heart, in review, J. Physiol. (2025).
- [37] U. Primessnig, P. Schönleitner, A. Höll, S. Pfeiffer, T. Bracic, T. Rau, M. Kapl, T. Stojakovic, T. Glasnov, K. Leineweber, P. Wakula, G. Antoons, B. Pieske, F.R. Heinzel, Novel pathomechanisms of cardiomyocyte dysfunction in a model of heart failure with preserved ejection fraction, Eur. J. Hear. Fail. 18 (8) (2016) 987–997
- [38] U. Primessnig, T. Bracic, J. Levijoki, L. Otsomaa, P. Pollesello, M. Falcke, B. Pieske, F.R. Heinzel, Long-term effects of Na+/Ca²⁺ exchanger inhibition with ORM-11035 improves cardiac function and remodelling without lowering blood pressure in a model of heart failure with preserved ejection fraction, Eur. J. Hear. Fail. 21 (12) (2019) 1543–1552.
- [39] S. Despa, F. Brette, C. Orchard, D. Bers, Na/Ca exchange and Na/K-ATPase function are equally concentrated in transverse tubules of rat ventricular myocytes, Biophys. J. 85 (5) (2003) 3388–3396.
- [40] P. Dan, E. Lin, J. Huang, P. Biln, G.F. Tibbits, Three-dimensional distribution of cardiac Na+-Ca2+ Exchanger and ryanodine receptor during development, Biophys. J. 93 (7) (2007) 2504–2518.
- [41] D.R. Scriven, P. Dan, Distribution of proteins implicated in excitation-contraction coupling in rat ventricular myocytes, Biophys. J. 79 (5) (2000) 2682–2691.
- [42] D. Sato, S. Despa, D.M. Bers, Can the sodium-calcium exchanger initiate or suppress calcium sparks in cardiac myocytes? Biophys. J. 102 (8) (2012) L31 – L33
- [43] T. Schendel, R. Thul, J. Sneyd, M. Falcke, How does the ryanodine receptor in the ventricular myocyte wake up: by a single or by multiple open L-type Ca2+channels? Eur. Biophys. J. 41 (1) (2012) 27–39.